



Cooling performance of film-cooling holes fed by channels of various shapes

Emma M. Veley^{*}, Karen A. Thole

Pennsylvania State University, 3127 Research Drive, State College, PA 16801, United States

ARTICLE INFO

Keywords:

Film cooling
Flow characteristics
Heat transfer
Gas turbines

ABSTRACT

Internal and external cooling is pertinent to maintaining operable surface temperatures of hot-section gas turbine components. Film cooling on the external surfaces is supplied from cooling passages placed inside of the blades and can affect the external film-cooling performance. Assessing internal cooling designs that were once difficult to investigate because of the complexity and costs of manufacturing cast turbine blades is now possible to more quickly and less costly through additive manufacturing (AM).

This paper provides results and analysis of an experimental and computational study of the cooling performance of meter-diffuser shaped film-cooling holes fed by a range of individual channel shapes with different cross-sectional shapes: circle, hexagon, pentagon, ellipse, diamond, square, rectangle, trapezoid, triangle – vertex up, and triangle – vertex down. These geometries were made possible through the use of AM. The perimeter, and consequently the surface area of the supply channels to the cooling holes, was maintained constant between the different channel shapes. The predictive computational results showed that the shape of the channel affects the secondary flows through the hole that in turn affects the overall film cooling as determined experimentally. The triangle – vertex up created flow structures in the diffuser-shaped cooling hole that caused the coolant jet to create a film on the surface with wide lateral spread; whereas the triangle – vertex down created flow through the cooling hole that caused the jet to fully detach at the same blowing ratio. Consequently, the triangle – vertex up had a 14% improvement in overall effectiveness over the triangle – vertex down and a 33% improvement over the circle which had the lowest overall effectiveness of all the tested shapes.

1. Introduction

To increase the thermal efficiencies of gas turbine engines, current operating temperatures are beyond the softening temperatures of airfoil materials [1]. For these hot-section components in gas turbine engines, cooling is essential to keep the components from melting during operation. Both internal and external cooling are used to protect and preserve the components. Internal cooling comes from passages within the components. To create external cooling, air is passed from the internal passages through holes in the wall to the external side, which is known as film-cooling. The coolant creates a film of cooling air around the component which is a barrier between the surface and the hot gas path temperatures. This film cooling is dependent both on the shape of the cooling hole that passes coolant to the surface [2–7] and on the supply channel [8–14].

The effect of supply channels feeding film cooling holes has been examined with holes fed from plenums [12,14,15], rectangular ducts

[8–10,14], and ribbed channels [10,16–18]. Several of these studies [9, 12,14] have shown that different feed directions into the hole result in variations in film-cooling performance for the same operating conditions. Kohli and Thole [14] saw that feeding shaped holes with a perpendicular cross-flow resulted in highly skewed cooling jets with peak levels of adiabatic effectiveness extending further downstream than the plenum fed jet, but with a narrower jet width. Both Hale et al. [12] and Stimpson et al. [9] saw lower film-cooling effectiveness for holes that were fed in a counter-flow configuration than those fed by a co-flow configuration. The counter-flow configuration had higher turning angles that resulted in separation within the hole, which then caused the counter-flow coolant jet to be more prone to lift off than the co-flow configuration hole.

Secondary flows within a hole impact the cooling jet and consequently affect the cooling performance. Holes with diffusers have been shown to improve the adherence of the cooling jet to the wall as a result of the lower momentum flux of the jet for a given mass flow rate [2,19]. The diffuser decreases the momentum through the hole and thereby

^{*} Corresponding author.

E-mail addresses: emv53@psu.edu (E.M. Veley), kthole@psu.edu (K.A. Thole).

<https://doi.org/10.1016/j.ijheatmasstransfer.2023.124561>

Received 9 June 2023; Received in revised form 19 July 2023; Accepted 31 July 2023

Available online 17 August 2023

0017-9310/© 2023 Elsevier Ltd. All rights reserved.

Nomenclature			
A_c	cross-sectional flow area	VR_{jet}	velocity ratio of the average coolant jet to mainstream
A_{min}	minimum cross-sectional area of cooling hole meter	X	streamwise distance
AR	Area Ratio of hole exit to hole inlet	Y	vertical distance
D	film cooling hole metering diameter	z	surface height
D_h	hydraulic diameter, $4A_c/p$	<i>Greek</i>	
DR	density ratio, ρ_c/ρ_∞	α	injection angle
FP	mass flow parameter, $\dot{m}_f(RT_c)^{0.5}/P_c A_{min}$	β	diffuser angles
h	convective heat transfer coefficient	θ	non-dimensionalized temperature, $(T_\infty - T)/(T_\infty - T_c)$
L	cooling hole length	ν	kinematic viscosity
k	thermal conductivity	ρ	fluid density
\dot{m}	mass flow rate	ϕ	overall effectiveness, $(T_\infty - T_s)/(T_\infty - T_c)$
M	blowing ratio, $(\dot{m}_f/A_{min})/(\rho_\infty U_\infty)$	$\bar{\phi}$	laterally averaged overall effectiveness
Ma	Mach number	$\bar{\phi}$	area-averaged overall effectiveness
N	number of surface point locations	ϕ_0	overall effectiveness without film cooling
P	pitch hole spacing	<i>Subscripts</i>	
P_c	static pressure at inlet of cooling hole	c	coolant
p	perimeter	d	downstream of cooling hole inlet
PR	pressure ratio, P_c/P_∞	f	film
R_a	arithmetic mean roughness, $\frac{1}{N} \sum_{j=1}^N z_j - z_{ref} $	i	coupon internal channel
Re	Reynolds number, $(4\dot{m})/(p\mu)$	j	index
S	spanwise direction	m	metering section
t	hole breakout width	ref	reference height
T	temperature	s	coupon surface
U	maximum/centerline velocity	u	upstream of cooling hole inlet
V	mass average velocity	∞	mainstream
VR_{ch}	velocity ratio of supply channel to mainstream		

reduces penetration of the jet into the mainstream flow [19]. Lateral diffusion is especially beneficial for two reasons. First, lateral diffusion causes greater coverage and therefore has a better uniformity in cooling. Second, because for jets in cross-flow, a counter-rotating vortex pair naturally forms [20] which encourages jet lift-off. As the coolant jet diffuses laterally, an anti-rotating vortex can form between the naturally forming counter-rotating vortex, thereby reducing the jet lift-off effect from the counter-rotating vortex pair and allowing the jet to remain attached to the wall [2].

Secondary flows in the cooling holes are also impacted by the flows from the supply channel. Nikuradse and Prandtl independently noted two types of secondary flow, one kind that is driven by pressure gradients and a second kind that is driven by shear stresses [21]. Secondary flows of the first kind have been extensively studied [8,16–18] with respect to film-cooling effectiveness, because these types of secondary flows occur around ribs which are a common augmentation feature for internal turbine cooling. The stress induced secondary flows of the second kind occur in turbulent flow within non-circular channels. To the authors' knowledge, although non-circular supply channels are common for film cooling such as in double-wall cooling schemes, the effects of secondary flows of the second kind on film-cooling effectiveness have not been studied. For internal concave corners in non-circular channels, secondary flows of the second kind cause the flow to impinge on the corner of the channel then follow the wall away from the corner until turning towards the center of the channel when the flow has its lowest momentum [21–23]. These secondary flow velocities are typically less than 3% of the bulk motion velocity [21,23]. The flow distribution in non-circular channels creates non-uniform heat transfer on the surface, with the corners providing less heat transfer than other regions along the wall [24]. Variations in surface roughness can also induce secondary flows of the second kind [21].

The inherent roughness from additive manufacturing can cause variations in heat transfer performance. For non-circular channels, Wildgoose and Thole [25] found that two AM channels with the same

cross-section but arithmetic mean roughness values that differed by a factor of three had very different friction and heat transfer performances. Specifically, at a Reynolds number of 20k, the rougher channel had a friction factor nearly 40% larger than the smoother channel and a Nusselt number almost 10% larger. AM roughness also affects the performance of film-cooling holes by increasing the in-hole convection and decreasing the cooling from the jet by increasing the likelihood of jet detachment, external mixing, and in-hole warming [26].

The purpose of the study reported in this paper is to examine the effect of different shaped channels on film-cooling performance of 7-7-7 holes. The ten channel shapes – circle, hexagon, pentagon, ellipse, diamond, square, rectangle, trapezoid, triangle – vertex up, and triangle – vertex down – are the same shapes as reported by Wildgoose and Thole [25]. Each AM test coupon had nine channels of the same shape with each channel supplying a single 7-7-7 hole. These ten simple shapes could be implemented in double-wall cooling schemes, but little is known about the impact of these shapes on the film cooling performance. The research presented in this article uniquely examines these shaped supply channels effect on the cooling jet. To examine these effects, both experiments and computational fluid dynamics (CFD) were used to examine the effects of the channel shape, internal Reynolds number, and blowing ratio on the overall cooling performance.

2. Experimental and computational approaches

This section discusses the general geometry studied as well as the experimental and computational methodologies used to study the effects of various shapes on cooling performance.

2.1. Geometric description

Ten test coupons were additively manufactured with meter-diffuser shaped film-cooling holes fed by individual supply channels. Fig. 1(a) shows the external coupon geometry which was the same for all test

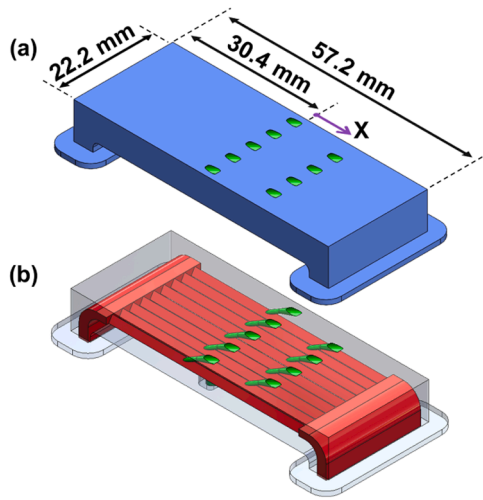


Fig. 1. Test coupon (a) external dimensions and (b) internal geometry.

coupons, and Fig. 1(b) shows an example of the internal geometry. Two rows of film-cooling holes were used to maintain conventional pitch-wise spacings and channel sizes that are found in modern turbine blades. Each coupon had feed channels with a different shaped cross-section: circle, hexagon, pentagon, ellipse, diamond, square, rectangle, trapezoid, triangle – vertex up, and triangle – vertex down. These are the same channels shapes used by Wildgoose and Thole [25] for internal cooling studies. The perimeter of each channel was kept constant (4.8 mm) to maintain the same convective surface area between each channel design. A consequence of maintaining the perimeter is that the cross-sectional flow areas and therefore the hydraulic diameters are not the same between channel shapes. The circle has the largest cross-sectional area of all the channels and the two equilateral triangle shapes have the smallest as given in Table 1 with the geometric

Table 1
Channel shape dimensions.

Shape	D_h [mm]	A_c [mm ²]	Relative to D
circle	1.53	1.84	
hexagon	1.39	1.49	
pentagon	1.32	1.42	
ellipse	1.28	1.39	
diamond	1.20	1.44	
square	1.20	1.44	
rectangle	1.06	1.15	
trapezoid	1.11	1.03	
triangle – vertex up	0.92	0.99	
triangle – vertex down	0.92	0.99	

parameters referenced to the cooling hole metering diameter ($D = 0.76$ mm).

Each test coupon had nine channels of the same cross-sectional shape. Each channel fed a single diffused film-cooling hole geometry referred to as the 7-7-7 hole. The 7-7-7 hole is a meter-diffuser shaped hole designed by Schroeder and Thole [4] with 7° lateral expansion angles and a 7° forward expansion angle. To maintain the hole spacing of $P/D = 6$ within a row of holes, each coupon had two rows of holes with five holes in the 1st row at $X/D = 0$ and four holes in the 2nd row at $X/D = 15$ offset from the 1st row by $S/D = 3$. The hole parameters are summarized in Table 2.

The wall thickness, defined as the distance between the top external surface and the top point of the internal channel as can be seen in Fig. 1 (b), and was maintained at three cooling hole metering diameters ($3D$) for all ten geometries. Subsequently for geometries that did not have flat surfaces on the top of the channel, the junction between the cooling holes and the shaped channels were complex with the lateral sides of the metering sections on some of the holes extending further upstream than the holes that intersect with a flat surface. These holes with inlet sides that extend laterally are especially prominent with the junction for the triangle – vertex up channels, where the sides extend almost an extra diameter upstream of the intersection at the top of the channel, which can be seen in Fig. 1(b). These extended sides create a diffuser like region at the inlet of the cooling hole and also extend the region impacted by in-hole convection upstream.

All ten coupons were additively manufactured out of Inconel 718 on an EOS M280 with a 40 μ m layer height. The cooling holes were oriented perpendicular to the substrate because this orientation has been seen to create a hole most faithful to the design intent [27]. Because of the hole orientation and the injection angle (30°), the shaped supply channels were built with their axis 60° to the substrate.

To estimate the as-built surfaces of the test coupons, an additional coupon was additively manufactured at 60° with nine channels, one of each channel shape except the triangle – vertex down. Computed tomography (CT) scans of these channels were used to estimate how well the channels in the test coupons were built as the separate part is assumed to have similar channel surface roughness as the film cooling coupons. The voxel size from the scan is 35 μ m. The postprocessing software resolves the surface to 3.5 μ m (1/10th voxel size) [28]. The surfaces determined from the CT scans were used to estimate the cross-sectional areas of the channels and the arithmetic mean roughness (R_a) in the channels. The cross-sectional area was determined from an average of a couple hundred slices along the length of the channel. R_a was determined differently for curved surfaces than for planer surfaces. For the curved surfaces of the circle and ellipse, an ellipse was fitted to each of the couple hundred slices along the length of the channels. The fitted ellipse was the surface from which the deviation was calculated for

Table 2
Cooling hole properties.

Parameter	7-7-7
Metering Diameter, D	0.762 mm
Lateral Expansion Angle, β_{lat}	7°
Forward Expansion Angle, β_{fwd}	7°
L/D	6
L_m/D	2.5
Injection Angle, α	30°
Coverage Ratio, t/P	0.35
Area Ratio, AR	2.5
Total # of Holes	9
# of 1 st row holes	5
# of 2 nd row holes	4
P/D in Row	6
P/D between Rows	3
2 nd row X/D	15
X/D hole centerline inlet	
1 st Row	-7.2
2 nd Row	7.8

the R_a for these two channels. The other seven channels had planes fitted to each side with a gaussian distribution. The deviation from the fitted planes was used to calculate R_a .

The results of the CT scans showed that the as-built cross-sectional areas were on average 7% larger than the design intents. Wildgoose and Thole [25] additively manufactured the same channels with the same process parameters at 90° (axis perpendicular to the substrate) and found that the average channel had cross-sectional areas 14% higher than the design intent. The area-weighted average R_a for each channel at 90° [25] and 60° is shown in Fig. 2. The area-weighted R_a values between the 90° and 60° channels are within the uncertainty of the roughness measurement for every channel, indicating that the differences in roughness between the downward and upward facing surfaces in the 60° channels cause the area-weighted R_a to be on the same order of magnitude of the 90° channel. The largest difference between the 90° channels and the 60° was the roughness on the downward facing walls in the 60° channels. The downward facing walls on the 60° channels had an average $R_a = 27.1 \mu\text{m}$ which was higher than the corresponding walls of the 90° channels with $R_a = 21.7 \mu\text{m}$. On the other hand, the upward facing walls in the 60° channels had average $R_a = 19.0 \mu\text{m}$ which was lower than the corresponding walls in the 90° channels with an $R_a = 23.5 \mu\text{m}$. With the results from each wall orientation, the area-averaged arithmetic mean roughness of the triangle – vertex down can be estimated to be $13.6 \mu\text{m}$ which is lower than the triangle – vertex up with an area-averaged $R_a = 14.9 \mu\text{m}$. This difference is a result of only one-third of the triangle – vertex down sides being downward facing surface whereas two-thirds of the triangle – vertex up sides are downward facing.

2.2. Experimental approach

The experiments for this study used the same test facility as described by Velely et al. [8] to experimentally examine 7-7-7 holes fed by the various shaped channels. The test section, shown in Fig. 3, uses the additively manufactured coupons interchangeably.

Across the top of the additive coupon is a mainstream flow path. The mainstream flow channel has an aspect ratio of $W/H = 2.7$ (25.4 mm x 9.5 mm) and is heated to 50°C using heaters upstream of the test section and pressurized to 360 kPa controlled by a pressure regulator upstream and a butterfly valve downstream of the test section. The mainstream channel was 38 times the mainstream channel hydraulic diameter prior to the test section to create hydraulically fully developed flow. The mainstream Mach number was 0.3 for all tests. The mainstream mass flow rate was measured upstream of the test section using a turbine flow meter. The test coupons were operated under conditions that created an engine relevant Biot number, $Bi = 0.2$, which is within the range of Biot numbers for turbine airfoils ($0.1 < Bi < 1$) [29]. The external heat transfer coefficient (h_{∞}) used to calculate Bi was derived from the CFD.

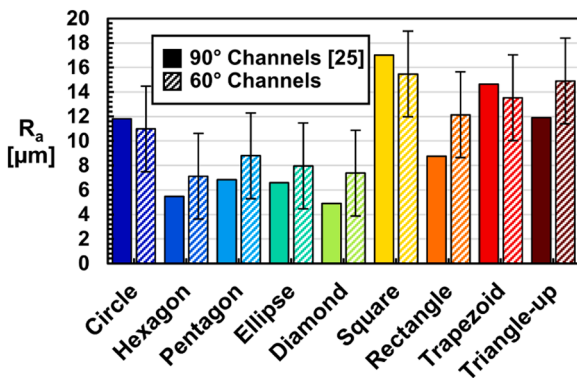


Fig. 2. Area-weighted arithmetic mean roughness of shaped channels built at 90° [25] and at 60°.

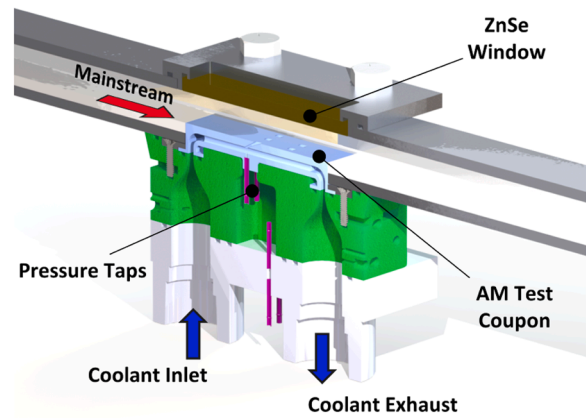


Fig. 3. Sectional view of the test section.

Coolant that was fed through the shaped internal channels was supplied through an instrumented plenum, which is shown in Fig. 3. The coolant gas was nitrogen at a temperature of -5°C (average of inlet and outlet plenum temperatures). The difference between the mainstream and coolant temperatures provided a coolant-to-mainstream density ratio (DR) of $DR = 1.2$. The coolant also had an upstream pressure regulator and a downstream valve to control the blowing ratio (M) and the internal downstream Reynolds number ($Re_{i,d}$). The coolant exhaust mass flow rate was measured using a laminar flow element. Both the blowing ratio and the internal downstream Reynolds number were varied for this study. Table 3 summarizes the test conditions used and includes the upstream internal Reynolds number ($Re_{i,u}$) which varies with M and the corresponding velocity ratios. The surface of the coupon was painted black to provide a high emissivity for the infrared camera measuring the surface temperature through the ZnSe window shown in Fig. 3. Surface thermocouples were used to calibrate the thermal images for each coupon. Each data set consists of an average of ten images to reduce precision uncertainty.

The blowing ratio was set based on a flow parameter (FP) curve produced prior to heat transfer tests. To create the flow parameter curves, all of the test coupons were supplied with a known mass flow rate and the pressure ratio (PR) across the 7-7-7 holes was measured. During the heat transfer tests the pressure ratio across the holes were adjusted until the mass flow rate that was calculated based on the corresponding flow parameter provided the desired blowing ratio. The flow parameter curves shown in Fig. 4 have some spread between the different supply channels. At $PR = 1.5$ the diamond has $FP = 0.67$ which is 13% higher than the circle with $FP = 0.59$. Overall, the channels with corners at the center of the cooling holes (diamond and triangle – vertex up) have higher flow parameters for a given pressure ratio than the corresponding channels (square and triangle – vertex down) with flat wall junctions with the hole. A possible reason for this trend is that the secondary flows of the second kind in the channels with upward

Table 3
Operating parameters.

M	VR_{jet}	$Re_{i,u}$ ($X/D < 0$)	$Re_{i,d}$ ($X/D > 15$)	$VR_{ch,u}$ min:max ($X/D < 0$)
0.26*	0.32	16.5k	14k	0.56:0.92
0.5*	0.61	18.5k	14k	0.63:1.04
0.7*	0.85	20k	14k	0.69:1.14
1	1.22	18k	9k	0.61:1.01
1*	1.22	23k	14k	0.78:1.29
1	1.22	27k	18k	0.92:1.52
1.5	1.83	27.5k	14k	0.93:1.54
2	2.44	32k	14k	1.09:1.80

* indicating the CFD cases

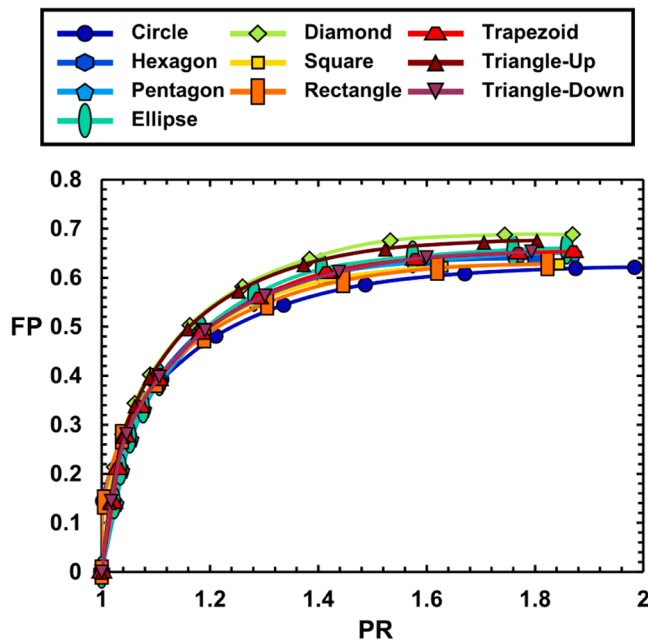


Fig. 4. Pressure ratio to flow parameter curves for 7-7 holes fed by all ten types of channels.

pointing corners direct the coolant from the supply channel to the center of the cooling holes providing some additional mass flow through the hole that is not pressure driven.

The absolute uncertainties for important parameters were calculated using the propagation of uncertainties method [30]. The uncertainty of M is 10% and is dependent on the uncertainties of PR and FP . The overall cooling effectiveness is dependent on the mainstream temperature (T_∞), the coolant temperature (T_c), and the surface temperature (T_s). At $\phi = 0.5$, the absolute uncertainty for ϕ is ± 0.02 . Repeatability testing was conducted using the circle coupon and the trapezoid coupon for at least one blowing ratio with three different Reynolds numbers. All the repeat test results were within the expected uncertainty of ϕ .

2.3. Computational approach

Conjugate steady Reynolds Average Navier Stokes (RANS) simulations were computed through the use of a commercial code [31] for the circle, square, trapezoid, triangle – vertex up, and triangle – vertex down. A coupled flow solver and the Reynolds-stress turbulence model with elliptic blending were used. The computational cases are denoted

in Table 3.

The boundary conditions were matched to the experiments, which are shown on the domain in Fig. 5(a). Symmetry planes at $S/D = 0$ and $S/D = 3$ were used to approximate the experimental coupons while reducing the size of the computational domain. The mainstream inlet used a velocity profile from a two-dimensional simulation of the upstream section of the test rig. The initial and inlet turbulence conditions were the software default. The mainstream outlet was a pressure outlet boundary condition. The coolant outlet mass flow rate was set for the downstream internal Reynolds number. The coolant inlet was a mass flow inlet that accounted for both the downstream internal Reynolds number and the blowing ratio. As a conjugate simulation, the solid was given the material properties of Inconel 718 including a thermal conductivity of 9.77 W/mK from an in-house measurement of an additively manufactured Inconel 718 test specimen.

Grid independence was investigated using the triangle – vertex up geometry because this geometry had the greatest complexity of the computationally simulated geometries. Three different grid resolutions were created with 4 million, 7 million, and 13 million cells. For all meshes, prism layers were used to resolve the boundary layer and to ensure the y^+ value of approximately one in the near wall region. The differences between the centerline and lateral averaged overall effectiveness results between all three meshes was less than 0.01. The middle mesh of 7 million cell mesh was selected to ensure that all any mesh sensitivity from other shape channels at the 4 million cells mesh size would be avoided. Fig. 5(b) shows the mesh of the triangle-vertex up on the 1st row hole symmetry plane. The remaining geometries had a similar number of cells using the same mesh settings. The simulations were considered converged when the surface average overall effectiveness changed by less than 0.001 over two-hundred iterations.

The computational setup was validated by comparing the computational results to the experimental results of the circle supply channel. Fig. 5(c) shows the augmentation in overall effectiveness from film cooling as a lateral average for the circle coupon for both the experiments and the CFD. The baseline effectiveness (ϕ_0) is from the circle channels with no film cooling holes at an internal Reynolds number of 14k and the film cooling overall effectiveness (ϕ) from the cases shown in Fig. 5(c) are at $M = 1$. The augmentation from film cooling is shown for comparison instead of just overall effectiveness because roughness inherent to AM changes the experimental convection coefficients compared to the smooth computational cases, therefore examining the augmentation from film cooling is a more accurate comparison. The lateral average in Fig. 5(c) shows that the CFD and experiments have augmentations within 10% over the region of interest. The greatest difference between the two curves occurs downstream of the 2nd row of holes, where the experimental results have a greater rate of decay from the film cooling than the CFD results. Roughness features in cooling

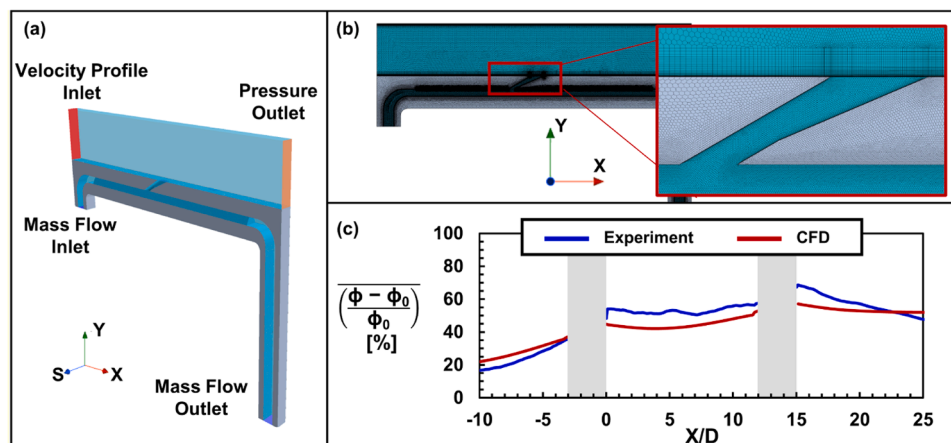


Fig. 5. The computational domain with (a) boundary conditions and (b) the mesh with a close view at the centerline of a cooling hole.

holes, like those found in AM holes, are known to reduce the film cooling performance compared to smooth holes [26].

3. Results and discussion

The results are presented in two sections. Section 3.1 focuses on the differences between shapes and how the resulting flow fields affect the overall effectiveness, Section 3.2 discusses the effects of variations in internal Reynolds number and blowing ratio on overall effectiveness.

3.1. Effect of supply channel shape

Fig. 6(a-j) shows contours of the overall effectiveness from the experiments at $M = 1$, $Re_{i,u} = 23k$, and $Re_{i,d} = 14k$ for all ten channel shapes. From these contours, the circle channel feed resulted in the lowest cooling effectiveness whereas the trapezoid and the triangle –

vertex up showed the highest cooling. As noted in Table 1 the circle also has the largest cross-sectional area while the trapezoid and triangles have the smallest cross-sectional areas of the tested geometries. The average velocity through each channel is inversely related to the cross-sectional area because $Re_{i,d}$ is maintained for all of these shapes. Consequently, the circle has the lowest average velocity through the supply channels, whereas the trapezoid and triangles have the highest average velocity of all the channels. The upstream channel velocity ratios ($VR_{ch,u}$) given in Table 3 have the minimum velocity ratio from the circle and the maximum velocity ratio from the triangles. The differences in velocity between the computationally simulated channels can be seen in the contours of the normalized velocity magnitude overlaid by velocity vectors at the centerline of the first row of 7-7-7 holes in Fig. 7 (a-e). The circle channel, shown in Fig. 7(a), is the only design computationally investigated that had an upstream ($X/D < -9$) normalized velocity magnitude of significantly less than unity, whereas the triangles

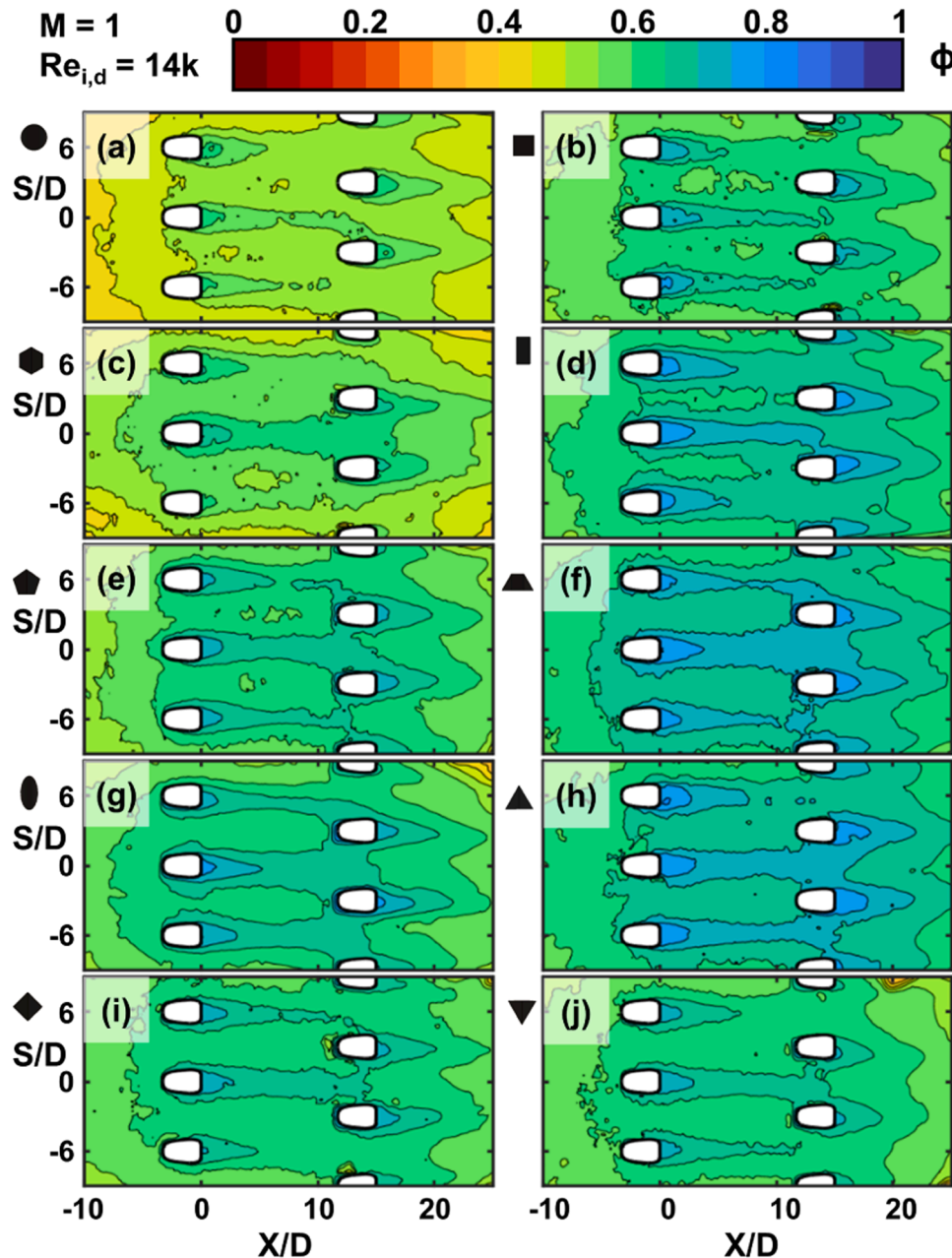


Fig. 6. Overall effectiveness contours at $M = 1$ and $Re_{i,d} = 14k$ for the (a) Circle, (b) Square, (c) Hexagon, (d) Rectangle, (e) Pentagon, (f) Trapezoid, (g) Ellipse, (h) Triangle – Vertex Up, (i) Diamond, and (j) Triangle – Vertex Down.

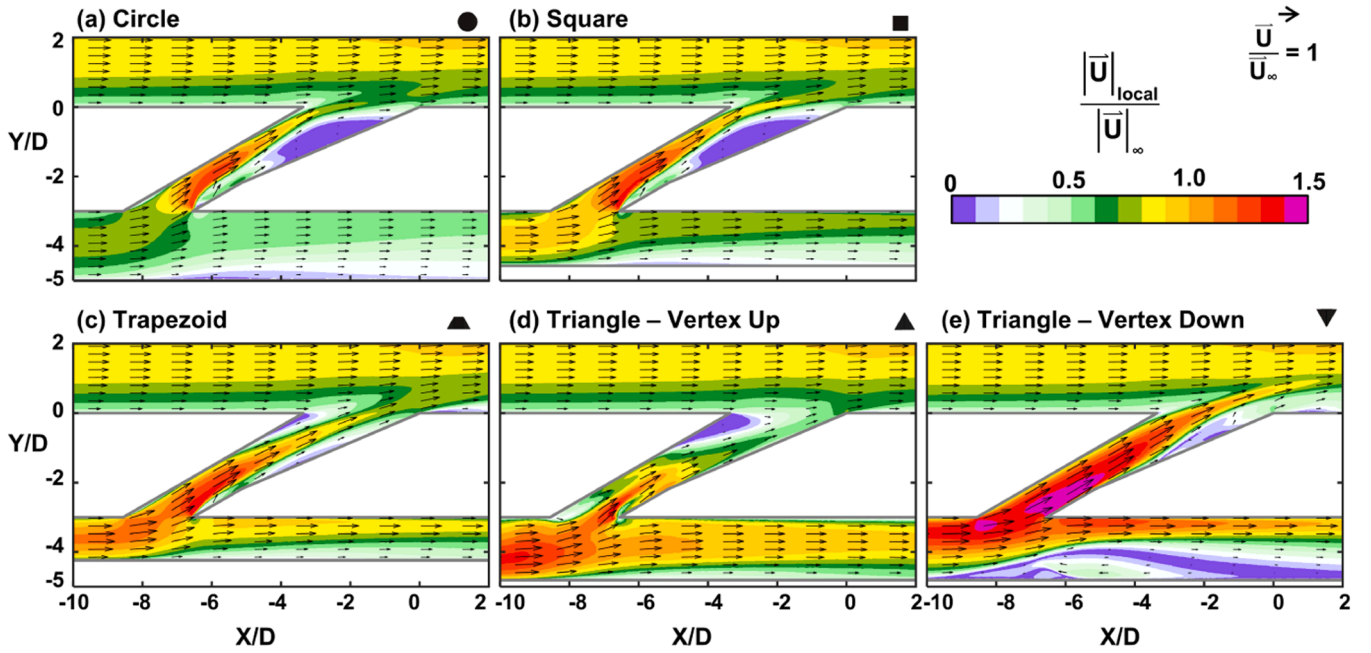


Fig. 7. Velocity contours with vector overlay at $M = 1$ and $Re_{i,d} = 14k$ from the CFD for the (a) Circle, (b) Square, (c) Trapezoid, (d) Triangle – Vertex Up, and (e) Triangle – Vertex Down.

have the smallest cross-sectional area of the tested shapes and consequently have regions of internal velocities upstream of the hole inlet of almost 50% more than the mainstream velocity. These variations in velocity affect the internal heat transfer coefficient; however, the secondary flows of the second kind also affect the heat transfer coefficient. The corners of the non-circular channels have a reduction in the heat transfer from the edges of the channel, thereby reducing the average heat transfer coefficient. The average internal heat transfer coefficients from the CFD were used to calculate the fin efficiency of the walls between the channels. Of the five shapes, the triangle – vertex up and triangle – vertex down had the highest fin efficiencies at 0.84 and 0.85, respectively; the square had the lowest fin efficiency at 0.80. These high fin efficiencies indicate that the walls between the channels were able to conduct the heat from the external surface to the bottom surfaces of the supply channels.

The effect from the channels alone can be seen upstream of the first row of hole in Fig. 6, with the circle in Fig. 6(a) having a lower effectiveness at $X/D = -10$ than any other coupon. The trapezoid and triangle – vertex up in Fig. 6(f) and Fig. 6(h) have the highest measured effectiveness. The trend in the upstream effectiveness between channel cross-sectional shapes is dependent on the surface area to flow volume ratio, the small differences in fin efficiency, and the average arithmetic mean roughness. The CFD only has the effects of the surface area to flow volume and fin efficiency, which results in a difference between the CFD and experimental results. As the traces of overall effectiveness in Fig. 8 (a) at $X/D = -10$ show, the CFD predicted that the triangle – vertex down to have a higher upstream effectiveness than the triangle – vertex up, a result of the triangle – vertex down having a large surface area at the nearest location to the surface thereby reducing the thermal resistance through the to the wall. However, as discussed in Section 2.1, the as-built surface of the triangle – vertex up is on average rougher than the triangle – vertex down, therefore causing the experimental triangle – vertex up to have a higher internal convection coefficient and therefore higher upstream effectiveness than the triangle – vertex down. The external heat transfer coefficient is also likely to be higher for the experimental cases than the CFD cases due to some external AM roughness which increase mixing in the boundary layer for the experiments. In turn the high external heat transfer coefficient causes the experimental effectiveness to be lower than the predicted CFD,

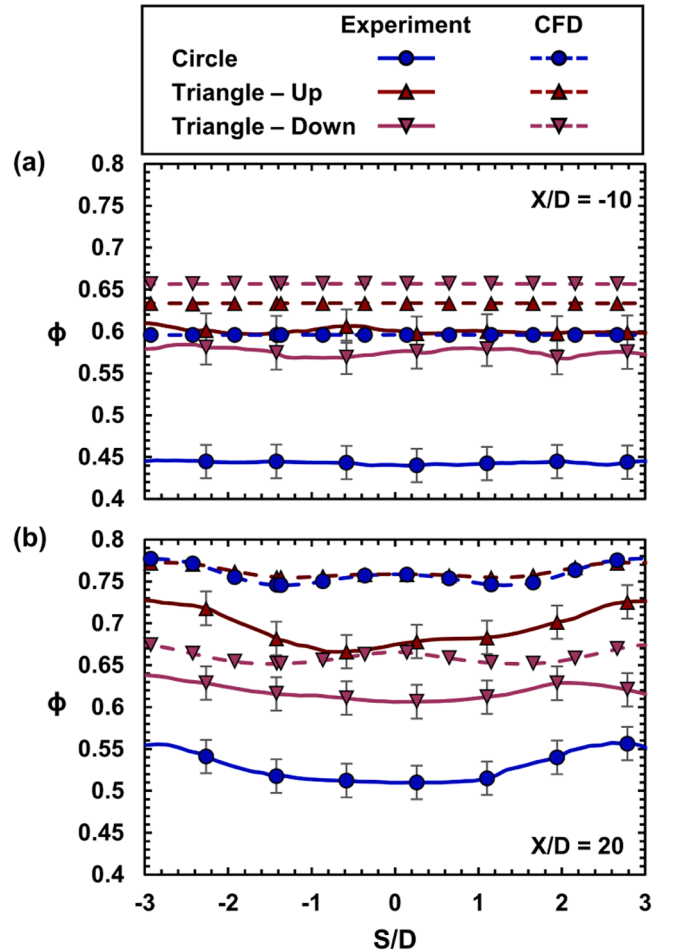


Fig. 8. Spanwise traces of the experimental and computational overall effectiveness at $M = 1$ and $Re_{i,d} = 14k$ for the circle, triangle – vertex up, and triangle – vertex down at (a) $X/D = -10$ and (b) $X/D = 20$.

especially in the case of the circle. The effects of the differences in heat transfer coefficients between the smooth CFD and the rough experiments can be seen to also impact the downstream effectiveness magnitudes as seen in Fig. 8(b). The differences between the smooth CFD results and rough experimental results highlight the importance of developing the ability to simulate the effects of large surface roughness in computational simulations.

The width of the coolant jets varies between supply channel shape as seen in Fig. 6 and in Fig. 8(b). The widths of the cooling jets were calculated by taking the location of 50% between the minimum and maximum effectiveness values from a trace such as those seen in Fig. 8(b). Specifically examining the width of the jet effectiveness width downstream of the second row of holes in Fig. 6, the hexagon fed holes had the lowest lateral spread (1.95D) of all the channels and the rectangle had the highest (2.71D). The circle and square have about the same lateral spread (2.36D), which also happened to be the average spread of all the holes. The triangle – vertex up has one of the wider lateral spreads (2.51D). The CFD underpredicted the width of the cooling jets as can be seen in the traces in Fig. 8(b). However, the CFD showed the same trends between channels as the experiments for the lateral spread such as the similarity between the circle and the square coolant jet width.

The lateral spread of the cooling jets is related to the flow through the cooling hole. Fig. 9 shows the normalized velocity magnitude at the inlet plane, the meter-diffuser intersection plane, and the breakout plane, providing the ability to examine the differences in lateral flow through the holes. The circle and the square, shown in Fig. 9(a-b), have very similar flow fields at the breakout plane. For both, the flow spreads laterally and favors the windward side of the holes. On the other hand, the triangle – vertex down, shown in Fig. 9(e), is also biased towards the windward side, but does not have notable lateral spread. Most of the flow is in the center of the hole resulting in a higher velocity as was also seen in Fig. 7(e). The trapezoid has flow biased on the leeward side of the diffuser, shown in Fig. 9(c). The flow from the triangle – vertex up is also biased on the leeward side of the diffuser and has good lateral spread and a lower velocity, as shown in shown in Fig. 9(d). Note that for the addition of additive roughness in the experiments, it is assumed based on the work of Banko et al. [32] that the momentum through all these holes is more centralized and uniform but still biasing to the same side of the diffuser (leeward vs windward) as the CFD shows.

The leeward bias and lateral diffusion in the triangle – vertex up fed hole shown in Fig. 9(d) directly impacts the lateral spread shown in both Fig. 6(h) and Fig. 8(b). The leeward biased and lateral diffusion of the flow results in a separation and recirculation on the windward side of the diffuser as seen in the velocity vectors of Fig. 7(d), and also provides a greater distance for the flow to diffuse than for windward biased flows that are seen in the circle and square shown in Fig. 7(a-b) and Fig. 9(a-b). The result of a windward biased flow of the circle and square was a

single counter-rotating vortex pair (CRVP) as shown in the secondary flow vectors of Fig. 10(d), which rotate in a direction that causes the coolant to be more prone to lift-off. However, the leeward biased flow with the greater diffusion length of the triangle – vertex up created two CRVPs, seen in Fig. 10(e), with the center CRVP pushing the coolant jet both down and laterally on the surface, thereby giving the triangle – vertex up the wide jet width seen in Fig. 10, Fig. 6(h) and Fig. 8(b). The trapezoid also had leeward biased flow at $M = 1$, but with less lateral diffusion than the triangle – vertex up as seen in Fig. 9(c). The centralized jet of the trapezoid resulted in less lateral diffusion and therefore only a single CRVP formed, similar to that of the circle shown in Fig. 10(d).

The triangle – vertex down in Fig. 8(b) has a flat effectiveness profile at $X/D = 20$ compared to the triangle – vertex up and circle. The relatively flat profile is likely caused by jet lift-off which was seen in the CFD velocity profile shown in Fig. 7(e). The flow through the hole fed by the triangle – vertex down has a high velocity through the center of the hole that is not seen in any of the other computationally simulated holes shown in Fig. 7(a-d). The high central velocity of the triangle – vertex down also results in less lateral spreading with the diffuser of the hole than the other examined holes, as seen in the normalized velocity contours through the hole in Fig. 9(e). This strong central jet through the hole results in a strong counter-rotating vortex pair (CRVP), which can be seen in the isosurfaces of q -criterion in Fig. 10(c) and in the secondary flow vectors in Fig. 10(f). As shown by the non-dimensional temperature contours in Fig. 10(c), the CRVP lifts the coolant off the surface which is detrimental to the overall effectiveness. In fact both the CFD and the experimental results in Fig. 8(a) and Fig. 8(b) show that the benefit from film cooling for the triangle – vertex down is only about a 5% increase in effectiveness at $X/D = 20$ over $X/D = -10$. Examining the effectiveness further downstream ($X/D \geq 25$) in Fig. 6(j) and Fig. 10(c) indicates that the small benefit from the film cooling quickly decreases and the overall effectiveness is lower than it was at $X/D = -10$.

It should be noted that the far downstream region ($X/D > 15$) has a lower internal Reynolds number than the upstream region ($X/D < 0$). When the $Re_{i,d}$ and M were maintained between geometries and at the same blowing ratio between coupons, the upstream Reynolds numbers ($Re_{i,u}$) were also the same between geometries. Because of the two rows of holes, there are three distinct regions of internal Reynolds number. The region downstream of the 2nd row of holes is where the internal Reynolds number for all nine channels is set as a common boundary condition between geometries. There is a small difference ($< 3\%$) in Reynolds numbers between channels that feed different rows of hole due to the small amount of pressure drop between the rows. The second region is upstream of both rows of holes. Upstream of the hole each channel must carry enough coolant to maintain both the downstream internal Reynolds number and the blowing ratio through the holes. For example to achieve $M = 1$ and $Re_{i,d} = 14k$, $Re_{i,u}$ must be 23k as is indicated by

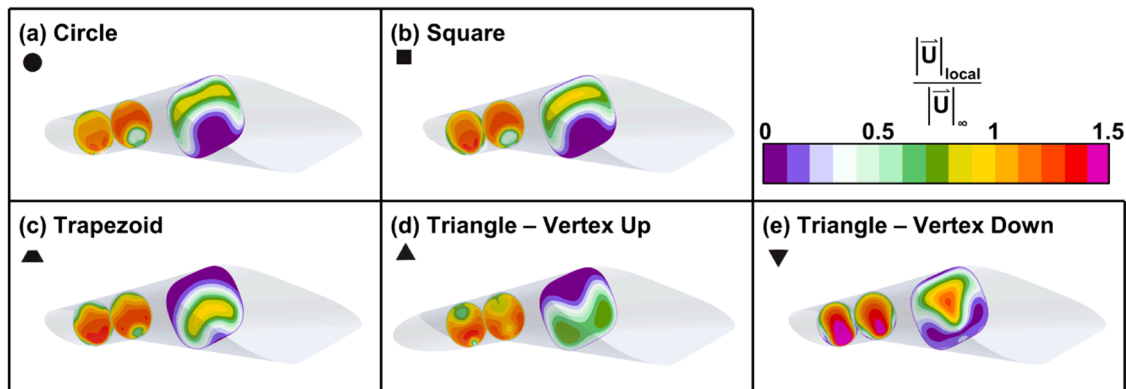


Fig. 9. Normalized momentum through the 1st row 7-7-7 holes at $M = 1$ from the CFD for the (a) Circle, (b) Square, (c) Trapezoid, (d) Triangle – Vertex Up, and (e) Triangle – Vertex Down.

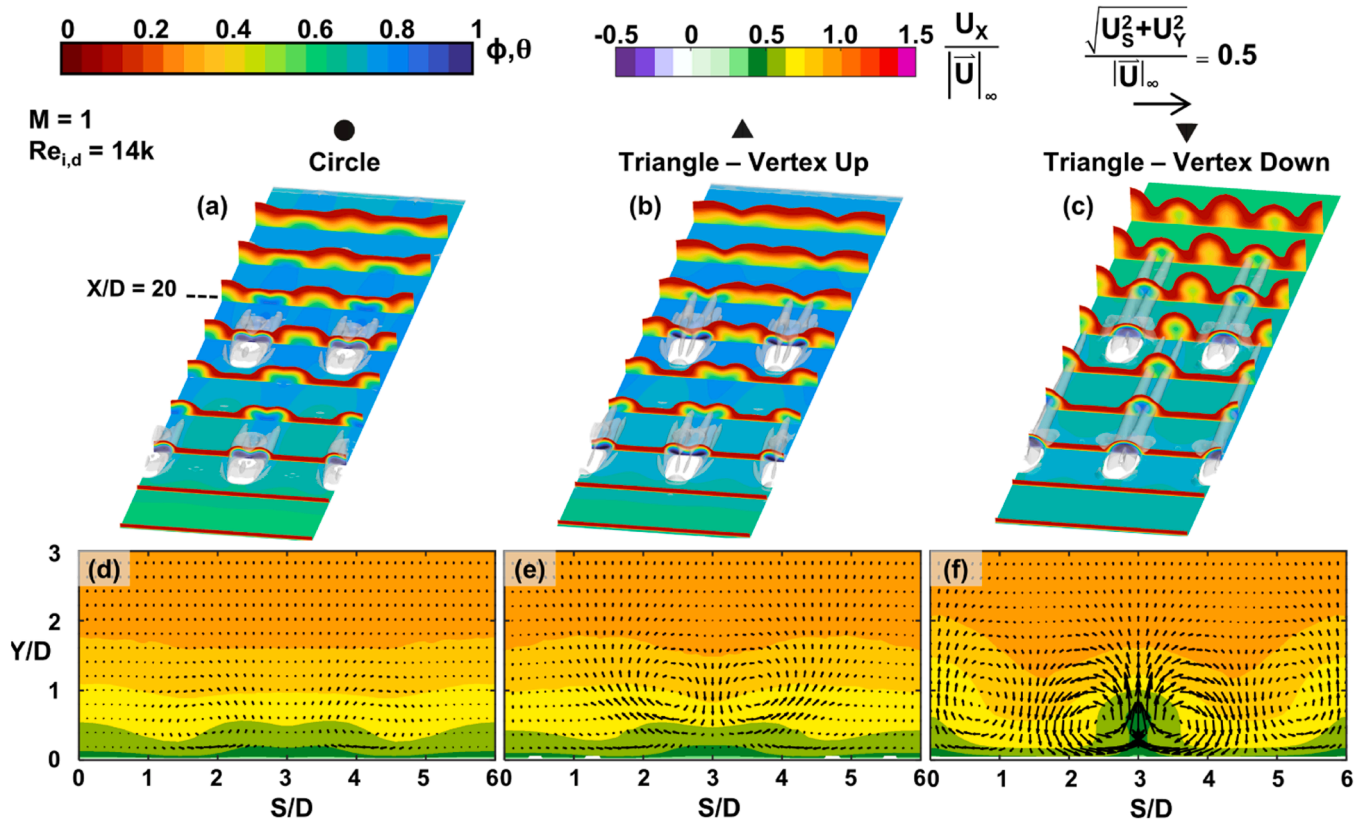


Fig. 10. From the $M=1$ and $Re_{i,d} = 14k$ computational simulations (a-c) contours of ϕ , contours of mainstream θ (> 0.1), and isosurfaces of Q -criterion ($@ 5 \times 10^7 \text{ s}^{-2}$) from the CFD for the (a) Circle, (b) Triangle – Vertex Up, and (c) Triangle – Vertex Down, and (d-f) contours in the spanwise plane of normalized streamwise velocity overlaid with vectors showing the secondary flows structures at $X/D = 20$ for (d) Circle, (e) Triangle – Vertex Up, and (f) Triangle – Vertex Down.

Table 3. Consequently, in this second region upstream of both rows of holes, all nine channels have the same upstream internal Reynolds number. The third region is between the two rows of holes. In the region between the two rows of holes, the channels that feed 1st row holes have $Re_{i,d}$ and the channels that feed 2nd rows of holes have $Re_{i,u}$. The drop in the internal velocity after a cooling can be seen in the velocity contours of Fig. 7.

The regions between the holes ($0 \leq X/D \leq 15$) not only have cooling from the internal channels of different Reynolds numbers, but also film cooling from the 1st row of holes and conduction from in-hole cooling of the 2nd row of holes. The lateral average overall effectiveness for all ten channels at $M = 1$ and $Re_{i,d} = 14k$ are shown in Fig. 11. After the 1st row of holes ($0 \leq X/D \leq 7$) the overall effectiveness is dominated by the film cooling from the 1st row of holes. The flow downstream of the hole inlets ($X/D > 7$) in the supply channels in Fig. 7(a-e) skews towards the top surface, a result of the pressure gradient that occurs at the inlet of the hole. The triangle – vertex down, shown in Fig. 7(e), is the only channel to form a large recirculation zone on the bottom side of the channel ($-7 \leq X/D \leq 0$, $-4.8 \leq Y/D \leq -4$). The flow through the triangle – vertex down is naturally biased to the top two-thirds of the channel, therefore the pressure gradient that diverted the small amount of mass flow on the bottom one-third of the channel also causes flow from downstream to recirculate back to the region of the hole inlet. The skewedness of the flow through the channel has dissipated by $X/D = 7$ where the inlet of the 2nd row of holes occurs in the other channels. Along the length of the 2nd row of holes ($7 \leq X/D \leq 15$) the surface has the added benefit of the corresponding in-hole convection. The in-hole convection causes the overall effectiveness to increase along this region. The region along the 1st row of holes also shows an increase in overall effectiveness from the in-hole cooling. Because of the complex junction between the channel and the hole, some geometries experience the in-hole cooling further

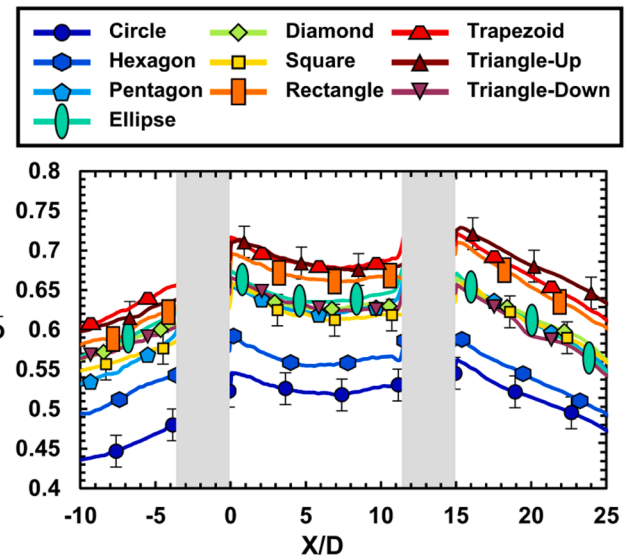


Fig. 11. Lateral-averaged overall effectiveness at $M = 1$ and $Re_{i,d} = 14k$ from the experiments for all ten channel shapes.

upstream than other designs.

The lateral averages in Fig. 11 show that the magnitude of the overall effectiveness immediately downstream from the 1st row of holes ($0 \leq X/D \leq 2$) is about the same as immediately downstream of the 2nd row of holes ($15 \leq X/D \leq 17$) for all ten channel shapes. Although the various geometries have coolant jets of differing widths, they have about the same rate of decay in effectiveness. These trends indicate that the

cooling in these regions is dominated by film cooling. However, after a few diameters downstream of the 1st row diffusers exits, the rate of decay decreases because of the different internal Reynolds numbers, whereas a downstream of the 2nd row of holes the decay rate is constant for the remaining ten metering diameters in the region of interest. Between the 1st and 2nd rows of holes, internal cooling from the channels and 2nd row of holes begins to dominate the overall effectiveness after $X/D = 5$, thereby decreasing the apparent decay of film from the 1st row holes.

In the lateral averages shown in Fig. 11, each channel shape falls into one of three groupings of cooling performance. When examining the area-averaged overall effectiveness downstream of the 2nd row of holes ($15 \leq X/D \leq 25$, $-9 \leq S/D \leq 9$), the hexagon only has a 4% increase in overall effectiveness over that of the circle which is within the range of experimental uncertainty ($\sim 5\%$). The second group contains the pentagon, ellipse, diamond, square, and triangle – vertex down. This second group of designs have an average of 18% higher overall effectiveness than the circle. The third group contains the rectangle, trapezoid, and triangle – vertex up which have an average 30% improvement in overall effectiveness over that of the circle. These groupings are not the same upstream of the 1st row of holes where the cooling is dictated by the internal cooling and the in-hole cooling.

3.2. Reynolds number and blowing ratio effects

All ten coupons were tested with three internal Reynolds numbers ($Re_{i,d} = 9k$, $14k$, and $18k$) at $M = 1$. These downstream Reynolds numbers correlate to $Re_{i,u} = 19k$, $24.5k$, and $29k$, respectively. Fig. 12 shows the lateral averages ($-9 \leq S/D \leq 9$) from the circle and pentagon at these three test conditions. The differences between internal Reynolds numbers have an effect less than the experimental uncertainty for regions that do not have a significant increase ($<50\%$) in $Re_{i,b}$ because differences between the Nusselt augmentation of internal channels decreases with increasing Reynolds number. Downstream of the 2nd row of holes is the only region where the differences in internal Reynolds number were greater than 50% between test cases. Therefore, only downstream of the 2nd row of holes ($S/D > 15$) have caused a change in overall effectiveness that was beyond the experimental uncertainty as seen in Fig. 12. Note that rate of decay is greater for the $Re_{i,d} = 9k$ case than the $Re_{i,d} = 18k$ case. Immediately out of the holes ($X/D = 15$) the coolant jet is dominating the surface cooling, but the internal convection for the $Re_{i,d} = 9k$ case provides less cooling than the $14k$ or $18k$ cases,

thereby causing the film for the $9k$ case to have greater thermal pickup along the streamwise direction resulting in the $9k$ case having greater decay rate than the $14k$ or $18k$ cases.

A large increase in internal Reynolds number is represented by the increase between $Re_{i,d} = 9k$ and $Re_{i,d} = 18k$, because the latter is twice the former. Fig. 13 shows the area-averaged effectiveness downstream of the 2nd row of holes ($15 \leq X/D \leq 25$) for the $Re_{i,d} = 9k$ and $Re_{i,d} = 18k$ cases. The circle had the highest percent increase in overall effectiveness between internal Reynolds numbers at almost 11% ($\phi_{Re=18k} - \phi_{Re=9k} = 0.052$), which directly corresponded to the increase in effectiveness of a separate coupon with circle channels and no film cooling holes. Once again, there is a trend between the internal cross-sectional area and the overall effectiveness; as the channel cross-sectional area increases the change in overall effectiveness also increases between Reynolds numbers. However, there is also a contributing factor of the film cooling which can be seen in the two triangle geometries. The triangle – vertex down has better internal cooling due to the large surface area of the channel near the external surface, but the triangle – vertex up has better film cooling flow dynamics as predicted by the CFD seen in Fig. 10. Consequently, the triangle – vertex up is less impacted by a change in internal Reynolds number compared to the triangle – vertex down. The triangle – vertex up has the lowest increase in overall effectiveness between Reynolds numbers ($\phi_{Re=18k} - \phi_{Re=9k} = 0.024$) which is slightly greater than the experimental uncertainty and results in only a 3.5% increase in overall effectiveness. Conversely, the triangle – vertex down has a 6.5% ($\phi_{Re=18k} - \phi_{Re=9k} = 0.037$) improvement between Reynolds numbers.

Moreso than the internal Reynolds number, the blowing ratio through the cooling holes also affects the overall effectiveness of each shape. The area-average overall effectiveness across a range of blowing ratios and $Re_{i,d} = 14k$ for all ten shapes is shown in Fig. 14. Across the range of tested blowing ratios, The trapezoid and triangle – vertex up have consistently high overall effectiveness compared to other shapes. Most of the channels either reach their highest overall performance at $M = 1$ or increase very little in performance with increasing blowing ratios ($M > 1$), which has been very commonly seen with additively manufactured film cooling holes [9,26,33]. The circle has relatively low overall effectiveness compared to the other shapes across the tested

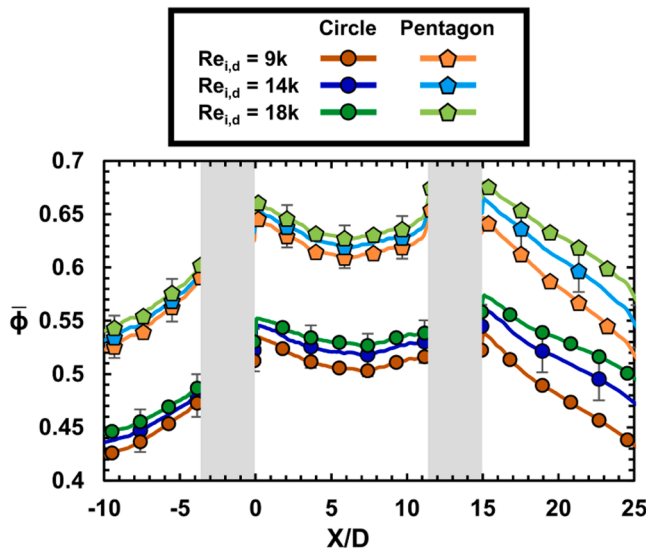


Fig. 12. Lateral averaged overall effectiveness of the experimental results of the Circle and Pentagon at three internal Reynolds numbers and $M = 1$.

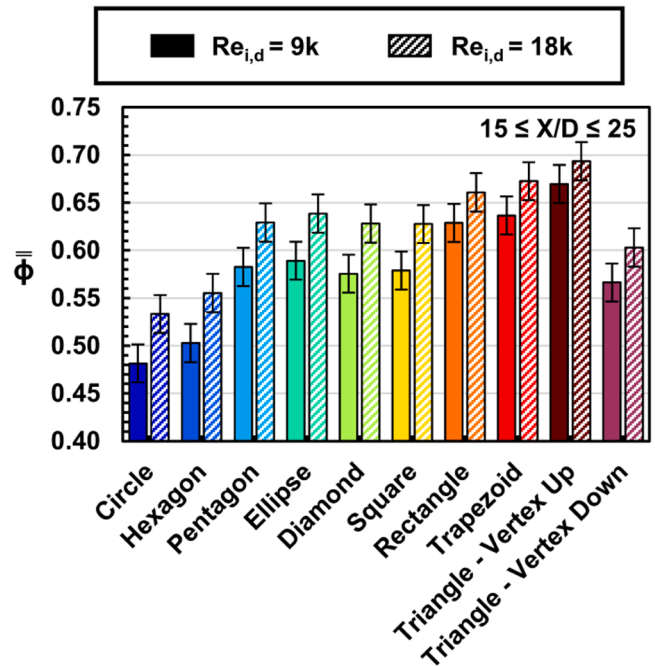


Fig. 13. Area-averaged overall effectiveness downstream of the 2nd row of holes for $M = 1$ at $Re_{i,d} = 9k$ and $18k$ for all ten channel shapes.

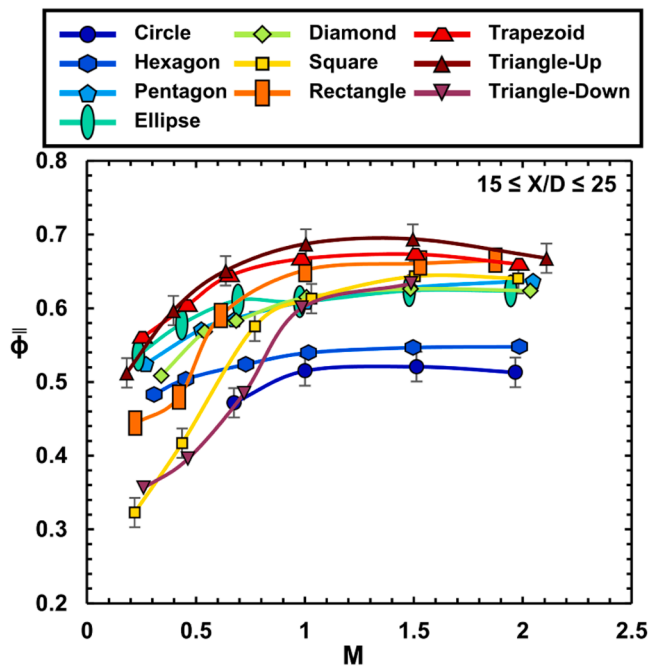


Fig. 14. Area-averaged overall effectiveness of the 2nd row ($15 \leq X/D \leq 25$) from the experiments of all ten channel shapes across a range of blowing ratios with $Re_{i,d} = 14k$.

blowing ratios except the hexagon which has similar effectiveness at $M \geq 1$.

The rectangle and the triangle – vertex down show a different trend over the range of tested blowing ratios than the other shapes. Both the rectangle and the triangle – vertex down have inflection points in the area-averaged effectiveness trends as seen in Fig. 14. The inflection point on both curves is at approximately $M = 0.5$. To investigate the source of the inflection point, computational simulations were run at lower blowing ratios for the triangle – vertex down. The lower blowing ratio simulations were also run for the triangle – vertex up to provide a comparison. In the triangle – vertex down, the flow at $M = 1$ is biased to the windward side of the hole as is shown in the normalized velocity magnitude contours through the hole in Fig. 15(h). However, at $M = 0.26$, the flow fed from the triangle – vertex down is biased on the leeward side of the diffuser as is shown in Fig. 15(b). At $M = 0.5$ shown in Fig. 15(d), the core of the flow is near the center of the hole, slightly biased to the windward side. At $M = 0.7$ shown in Fig. 15(f), the core of the flow through the hole is completely biased on the windward side of the hole. For the triangle – vertex up, the flow is always biased on the leeward side of the hole regardless of the blowing ratio as seen in Fig. 15(a), (c), (e), and (g) and also has a lower relative velocity compared to the triangle – vertex down at the same blowing ratio. The switch in flow bias through the triangle – vertex down fed hole corresponds with the inflection point in the experimental results. The core of the flow through the hole changes sides because the secondary flows through the hole change. At $M = 0.26$, there is forward diffusion and some lateral diffusion on the leeward diffuser wall and a weak vortex pair on the windward wall (not shown). Increasing the blowing ratio to $M = 0.5$, the vortex pair has gained strength and moved to the lateral side walls of the diffuser. At this blowing ratio, there is still forward diffusion in the center third of the diffuser, but the vortex pair pulls the flow towards the windward side of the hole. At $M = 0.7$, a recirculation zone forms on the leeward wall of the diffuser. At $M = 1$, the recirculation region is smaller than the low blowing ratios, but the core of the flow is also centrally located on the windward side of the hole. For the triangle – vertex up, no clear vortices form at any blowing ratio, diffusion occurs along the leeward wall, and a separation zone occurs along the length of the

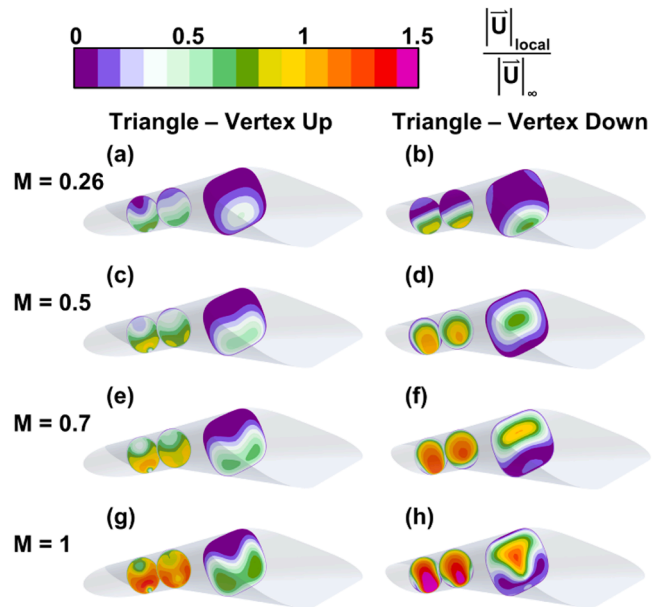


Fig. 15. The velocity at three planes through the 1st row cooling holes for the (a) Triangle – Up at $M = 0.26$, (b) Triangle – Down at $M = 0.26$, (c) Triangle – Up at $M = 0.5$, (d) Triangle – Down at $M = 0.5$, (e) Triangle – Up at $M = 0.7$, and (f) Triangle – Down at $M = 1$.

windward side of the hole.

4. Conclusion

The effect of ten different channel shapes on the overall effectiveness was examined using CFD and examined experimentally using AM test coupons. The perimeter, and consequently the surface area, was maintained between the various shaped channels. The differences in the channel cross sections altered the junction of the 7-7-7 cooling hole and the channel. Although the junction of the hole to coolant channels varied, experiments showed that the shape of the feed channel does not have a significant impact on the flow parameter through the cooling holes for a given pressure ratio.

Overall effectiveness measurements were made to determine the cooling performance of the various channel shapes. These experimental results showed a similar magnitude of the overall effectiveness between the two rows of holes for the same channel shape. The experimental overall effectiveness results showed an inverse relation between the overall effectiveness and the cross-sectional area of the channel. For two triangle channels which have the same cross-sectional area, the triangle – vertex up has a higher film cooling effectiveness than the triangle – vertex down, which indicates differences in the flow through the cooling holes. The computational work provided the ability to examine the flow physics through the holes. The secondary flows through the holes fed by the triangle – vertex down channels caused the cooling jet to lift-off the external surface; whereas the secondary flows through the holes fed by the triangle – vertex up creates a coolant jet that remains on the surface with good lateral spread.

Each of the ten channel shapes were also experimentally tested at three internal Reynolds numbers. The overall effectiveness was not sensitive to changes in internal Reynolds number less than 50%. Doubling the internal Reynolds number had the largest impact on the circle channel with over a 10% increase in the area-averaged overall effectiveness. The triangle – vertex up had the lowest improvement at 3.5% of all of the shaped channels, indicating designs that have superior film cooling are not as dependent upon small changes in the internal cooling as designs that initially have poorer film or internal cooling.

When testing all ten channels across a range of blowing ratios, the

experimental results showed that the triangle – vertex down and the rectangle have an inflection point in area averaged cooling performance around $M = 0.5$. Computational simulations of the triangle – vertex down at low blowing ratios ($0.26 \leq M \leq 1$) showed that this change in cooling performance was a result of the coolant in the diffuser changing from a bias on the leeward side at the blowing ratios below the inflection point to the windward side for blowing ratios above the inflection point. The change between sides of flow bias was a direct result of the secondary flows within the cooling hole fed by the triangle – vertex down channels.

In all, the secondary flows through cooling holes are dependent on the feed channel shape and, consequently, the coolant jet is also very dependent on the shape of the feed channel. The results of this study are important for understanding the importance of secondary flows in the feed channel on the ability of a cooling hole to create an effective film on the surface of a part. Therefore, designers should always design the supply channel and holes together and examine the combined performance for a range of operating conditions to develop the best cooling schemes for their application.

CRediT authorship contribution statement

Emma M. Veley: Data curation, Formal analysis, Writing – original draft, Writing – review & editing. **Karen A. Thole:** Writing – review & editing.

Declaration of Competing Interest

The authors declare that they have no known competing financial interests or personal relationships that could have appeared to influence the work reported in this paper.

Data availability

Data will be made available on request.

Acknowledgments

This paper is based upon work supported by the Department of Energy under Award Number DE-FE0025011. This report was prepared as an account of work sponsored by an agency of the United States Government. Neither the United States Government nor any agency thereof, nor any of their employees, makes any warranty, express or implied, or assumes any legal liability or responsibility for the accuracy, completeness, or usefulness of any information, apparatus, product, or process disclosed, or represents that its use would not infringe privately owned rights. Reference herein to any specific commercial product, process, or service by trade name, trademark, manufacturer, or otherwise does not necessarily constitute or imply its endorsement, recommendation, or favoring by the United States Government or any agency thereof. The views and opinions of authors expressed herein do not necessarily state or reflect those of the United States Government or any agency thereof.

Additionally, the authors would like to thank Mr. Leland Tien and Mr. Thomas Corbett for their assistance during the CFD development and Mr. Thomas Corbet for his assistance in preparing the final document.

References

- [1] D.G. Bogard, K.A. Thole, Gas turbine film cooling, *J. Propuls. Power.* 22 (2006) 249–270, <https://doi.org/10.2514/1.18034>.
- [2] B.A. Haven, D.K. Yamagata, M. Kurosaka, S. Yamawaki, T. Maya, Anti-kidney pair of vortices in shaped holes and their influence on film cooling effectiveness. Vol. 3 Heat Transfer Electric Power Industrial and Cogeneration, American Society of

Mechanical Engineers, Orlando, Florida, USA, 1997, <https://doi.org/10.1115/97-GT-045.V003T09A007>.

- [3] R.J. Goldstein, Film cooling, *Adv. Heat Transf.*, Elsevier (1971) 321–379, [https://doi.org/10.1016/S0065-2717\(08\)70020-0](https://doi.org/10.1016/S0065-2717(08)70020-0).
- [4] R.P. Schroeder, K.A. Thole, Adiabatic effectiveness measurements for a baseline shaped film cooling hole, *J. Turbomach.* 144 (2022), 121003, <https://doi.org/10.1115/1.4055271>.
- [5] J.C. Snyder, K.A. Thole, Performance of public film cooling geometries produced through additive manufacturing, *J. Turbomach.* 142 (2020), 051009, <https://doi.org/10.1115/1.4046488>.
- [6] F.B. Jones, D.W. Fox, T. Oliver, D.G. Bogard, Parametric optimization of film cooling hole geometry. Vol. 5A Heat Transfer — Combustors Film Cooling, American Society of Mechanical Engineers, Virtual, 2021, <https://doi.org/10.1115/GT2021-59326>. OnlineV05AT12A013.
- [7] F.B. Jones, T. Oliver, D.G. Bogard, Adjoint optimization of film cooling hole geometry. Vol. 5A Heat Transfer — Combustors Film Cooling, American Society of Mechanical Engineers, Virtual, 2021, <https://doi.org/10.1115/GT2021-59332>. OnlineV05AT12A014.
- [8] E.M. Veley, K.A. Thole, D.G. Bogard, The effects of channel supplies on overall film-cooling effectiveness, in: 2023: pp. GT2023-103136.
- [9] C.K. Stimpson, J.C. Snyder, K.A. Thole, D. Mongillo, Effects of coolant feed direction on additively manufactured film cooling holes, *J. Turbomach.* 140 (2018), 111001, <https://doi.org/10.1115/1.4041374>.
- [10] G. Wilfert, S. Wolff, Influence of internal flow on film cooling effectiveness, *J. Turbomach.* 122 (2000) 327–333, <https://doi.org/10.1115/1.555449>.
- [11] K.A. Thole, M. Gritsch, A. Schulz, S. Wittig, Effect of a crossflow at the entrance to a film-cooling hole, *J. Fluids Eng.* 119 (1997) 533–540, <https://doi.org/10.1115/1.2819277>.
- [12] C.A. Hale, M.W. Plesniak, S. Ramadhyani, Film cooling effectiveness for short film cooling holes fed by a narrow plenum, *J. Turbomach.* 122 (2000) 553–557, <https://doi.org/10.1115/1.1303705>.
- [13] D.G. Hyams, J.H. Leylek, A detailed analysis of film cooling physics: part III—streamwise injection with shaped holes, *J. Turbomach.* 122 (2000) 122–132, <https://doi.org/10.1115/1.555435>.
- [14] A. Kohli, K.A. Thole, Entrance effects on diffused film-cooling holes. Vol. 4 Heat Transfer in Electric Power Industry and Cogeneration, American Society of Mechanical Engineers, Stockholm, Sweden, 1998, <https://doi.org/10.1115/98-GT-402.V004T09A070>.
- [15] C.E. Bryant, J.L. Rutledge, A computational technique to evaluate the relative influence of internal and external cooling on overall effectiveness, *J. Turbomach.* 142 (2020), 051008, <https://doi.org/10.1115/1.4045987>.
- [16] D.W. Fox, F.B. Jones, J.W. McClintic, D.G. Bogard, T.E. Dyson, Z.D. Webster, Rib turbulator effects on crossflow-fed shaped film cooling holes, *J. Turbomach.* 141 (2019), 031013, <https://doi.org/10.1115/1.4041673>.
- [17] E. Sakai, T. Takahashi, Y. Agata, Experimental study on effects of internal ribs and rear bumps on film cooling effectiveness, *J. Turbomach.* 135 (2013), 031025, <https://doi.org/10.1115/1.4007546>.
- [18] R. Zhu, S. Li, G. Xie, Conjugate heat transfer and flow features of single-hole and combined-hole film cooling with rib-roughened internal passages, *J. Therm. Sci. Eng. Appl.* 14 (2022), 091006, <https://doi.org/10.1115/1.4053931>.
- [19] M. Gritsch, W. Colban, H. Schär, K. Döbbling, Effect of hole geometry on the thermal performance of fan-shaped film cooling holes, *J. Turbomach.* 127 (2005) 718–725, <https://doi.org/10.1115/1.2019315>.
- [20] T.F. Fric, A. Roshko, Vortical structure in the wake of a transverse jet, *J. Fluid Mech.* 279 (1994) 1–47, <https://doi.org/10.1017/S0022112094003800>.
- [21] N.V. Nikitin, N.V. Popelenskaya, A. Stroth, Prandtl's secondary flows of the second kind. Problems of description, prediction, and simulation, *Fluid Dyn.* 56 (2021) 513–538, <https://doi.org/10.1134/S0015462821040091>.
- [22] L. Prandtl, *Turbulent Flow*, Zurich, Germany, 1926. <https://ntrs.nasa.gov/api/citations/19930090799/downloads/19930090799.pdf>.
- [23] F. Deprati, Direct numerical simulation of flow and heat transfer in complex ducts, *Aerotec. Missili Spaz.* 100 (2021) 263–276, <https://doi.org/10.1007/s42496-021-00093-3>.
- [24] R.G. Deissler, M.F. Taylor, *Analysis of Turbulent Flow and Heat Transfer in Noncircular Passages*, National Aeronautics and Space Administration, Cleveland, Ohio, 1959.
- [25] A.J. Wildgoose, K.A. Thole, Heat transfer and pressure loss of additively manufactured internal cooling channels with various shapes, *J. Turbomach.* 145 (2023), 071011, <https://doi.org/10.1115/1.4056775>.
- [26] C.K. Stimpson, J.C. Snyder, K.A. Thole, D. Mongillo, Effectiveness measurements of additively manufactured film cooling holes, *J. Turbomach.* 140 (2018), 011009, <https://doi.org/10.1115/1.4038182>.
- [27] E.M. Veley, K.A. Thole, D.G. Bogard, Manufacturing quality of engine scale additively manufactured film cooling holes, (2022).
- [28] C. Reinhart, *Industrial CT & precision*, (2011).
- [29] T.E. Dyson, J.W. McClintic, D.G. Bogard, S.D. Bradshaw, Adiabatic and overall effectiveness for a fully cooled turbine vane. Vol. 3B Heat Transfer, American Society of Mechanical Engineers, San Antonio, Texas, USA, 2013, <https://doi.org/10.1115/GT2013-94928.V03BT13A037>.
- [30] R. Figliola, D. Beasley, *Theory and Design for Mechanical Measurements*, 6th ed., John Wiley & Sons, 2014.

- [31] Siemens digital industries software, Simcenter STAR-CCM+, (2021).
- [32] A.J. Banko, M.J. Benson, F.T. Davidson, W. Zia, A. Bordbar, C. Boyce, E.M. Veley, K.A. Thole, Effects of surface roughness on three-dimensional flow structure within shaped film cooling holes, in: 2023: pp. GT2023-104073.
- [33] E.M. Veley, K.A. Thole, M.T. Furgeson, D.G. Bogard, Printability and overall cooling performance of additively manufactured holes with inlet and exit rounding, J. Turbomach. 145 (2023), 031017, <https://doi.org/10.1115/1.4056389>.